minerals

MDPI

Article

Elucidating the Genetic Mechanism and the Ore-Forming Materials of the Kaladawan Iron Deposit in the North Altyn Tagn, Western China

Yuyao Chen [1], Yuting Cao [1,*], Liang Liu [2], Chao Wang [2], Wenqiang Yang [2], Yongsheng Gai [2], Tianhe Xie [1], Lihao Song [1] and Fei Xie [1]

[1] Shandong Provincial Key Laboratory of Depositional Mineralization & Sedimentary Minerals, College of Earth Science and Engineering, Shandong University of Science and Technology, Qingdao 266590, China; chenyuyao199988@outlook.com (Y.C.)
[2] State Key Laboratory of Continental Dynamics, Department of Geology, Northwest University, Xi'an 710069, China
* Correspondence: caoyuting@sdust.edu.cn

Abstract: The Kaladawan iron deposit is located in the North Altyn Tagh and exhibits occurrences of iron ore bodies at the contact zone between Ordovician magmatic rocks (basalts, rhyolite, and granodiorite) and marble. However, controversy persists regarding the genetic classification and metallogenic mechanism of this deposit. Through a field investigation, single mineral in situ geochemical analysis, whole-rock geochemical analysis, and Fe isotope determination, the following conclusions are made: (1) Ti-(Ni/Cr) and (V/Ti)-Fe diagrams indicate that the magnetite from all studied rocks underwent hydrothermal metasomatism, while (Ni/(Cr + Mn))-(Ti + V) and (Ca + Al + Mn)-(Ti + V) diagrams suggest a skarn origin for these magnetites. Therefore, it can be inferred that the Kaladawan iron deposit is skarn-type. (2) The iron ore exhibits similar rare-earth-element characteristics to the altered basalt. Additionally, the altered basalts (δ^{56}Fe = 0.024~0.100‰) are more enriched in light Fe isotopes than the unaltered basalts (δ^{56}Fe = 0.129~0.197‰) at the same location, indicating that the ore-forming materials of the Kaladawan iron ore are mainly derived from basaltic rocks. (3) According to the law of mass conservation and the intermediate Fe isotopic composition of the iron ore between the granodiorite and basalt, the hydrothermal fluid for the formation of iron ores was inferred to be derived from the late intrusive granodiorite.

Keywords: North Altyn Tagh; Kaladawan iron deposit; skarn deposit; Ordovician magmatic rocks; metallogenic mechanism

Citation: Chen, Y.; Cao, Y.; Liu, L.; Wang, C.; Yang, W.; Gai, Y.; Xie, T.; Song, L.; Xie, F. Elucidating the Genetic Mechanism and the Ore-Forming Materials of the Kaladawan Iron Deposit in the North Altyn Tagn, Western China. *Minerals* **2024**, *14*, 589. https://doi.org/10.3390/min14060589

Academic Editors: Evgeny Galuskin and Jaromír Leichmann

Received: 21 March 2024
Revised: 26 May 2024
Accepted: 30 May 2024
Published: 3 June 2024

1. Introduction

The Kaladawan Polymetallic Metallogenic Belt, located in the eastern section of the Altyn Mountains, falls within a polymetallic metallogenic subzone encompassing iron, copper, lead, gold, silver, and other valuable mineral resources. Since the 1960s, extensive geological research has provided comprehensive and systematic insights into the distribution characteristics of strata, intrusive rocks, volcanic rocks, metamorphic rocks, and mineral deposits in this region. However, due to the intricate nature of regional tectonic evolution and the ore genesis processes involved here, the genetic type and material source of the Kaladawan iron deposits are still controversial.

The Baba iron deposit in the Kaladawan was initially classified as a skarn-type iron deposit [1], according to an earlier survey. Qi et al. [2] proposed that it is actually a hypabyssal hydrothermal metasomatic filling iron deposit, influenced by regional fault structures caused by diabase magmatic–hydrothermal fluid. Based on the presence of numerous skarn minerals in the Kaladawan iron deposit and its association with lithological horizons, the Institute of Xinjiang Geological Survey [3] considers this deposit to be of

stratabound skarn type. Ni [4] concluded that the magnetite in the Kaladawan iron deposit formed through magmatic eruption, while the magnetite in basalt resulted from magmatic liquation. This suggests that the deposit is a late metamorphic transformation magnetite deposit superimposed on a magmatic liquation–ejection (overflow–intrusion) process. Hou et al. [5], based on deposits and occurrences in the Kaladawan area, classified it as a submarine volcanogenic iron oxide (SVIO) deposit. Guo [6] proposed that it is a volcanic eruption–magma hydrothermal reformation-enriched marine volcanic rock type, with its iron ore material derived from the Middle–Upper Ordovician Lapeiquan Formation's volcanic sedimentary rock series. Previous studies have suggested that the Kaladawan iron deposit is a result of volcanic sedimentary mineralization, with the primary ore-forming material derived from intermediate–basic magma. Additionally, the intrusion of intermediate–acid magma also provides a source for ore-forming materials and leads to the skarnization transformation [3,7–9]. An age comparison between hydrothermal titanite and garnet in the iron ore and surrounding rocks indicated a skarn-type [10].

In summary, there are still ongoing debates regarding the origin of the Kaladawan iron deposit, primarily focusing on three perspectives: volcanic sedimentary mineralization, followed by skarnization transformation; SVIO; and skarn-type. To elucidate the metallogenesis, this study conducted a comprehensive geochemical and Fe isotope analysis of whole rocks, as well as in situ magnetite geochemical analysis in various rock samples within the study area, thus helping to ascertain the sources of the ore-forming materials and enhancing the understanding of the processes by which the iron deposit is formed.

2. Geological Background

The North Altyn is situated between the northern side of the Altyn Tagh strike-slip fault and the east–west Altyn Tagh northern margin fault. It borders the southern margin of the Tarim block to the north and the Qaidam Basin to the south (Figure 1a) [11]. The Kaladawan district is located in the middle-eastern section of the North Altyn, which structurally belongs to the Hongliugou–Lapeiquan ophiolitic melange belt. The history of tectonic evolution in this region is highly complex, characterized by variable environmental conditions and multiple cycles of magmatism, with particularly intense magmatism during the late Mesoproterozoic and middle-to-late Paleozoic periods. Diverse types and degrees of metamorphism are observed here, forming a sequence of volcanic–sedimentary–metamorphic rocks (Figure 1b) [1,6,12].

Previous studies have indicated that the early Paleozoic period was a crucial phase of magmatic activity in the Kaladawan district and its surrounding areas. During this stage, there was a bimodal volcanic eruption within a rift environment, resulting in the formation of bimodal volcanic rocks. Subsequently, numerous intermediate–acid intrusive rocks and basic–ultrabasic intrusive rocks were generated [13–18]. A majority of intrusive rocks were formed during the late Proterozoic and late Paleozoic periods. The late Proterozoic intrusive rocks consist of gabbro, diorite, and granodiorite, all of which are small rock stocks or dykes. The late Paleozoic is characterized by intermediate–acid intrusive activity, with the spatial distribution of magmatic rocks controlled by the Altyn Tagh fault zone. The intermediate–acid plutonic rocks are widely distributed and occur as large-scale apophyses or batholiths, including quartz diorite, granodiorite, porphyritic plagioclase granite, and granite porphyry. The late Proterozoic and Paleozoic dikes mainly comprise basic, intermediate, and acid compositions.

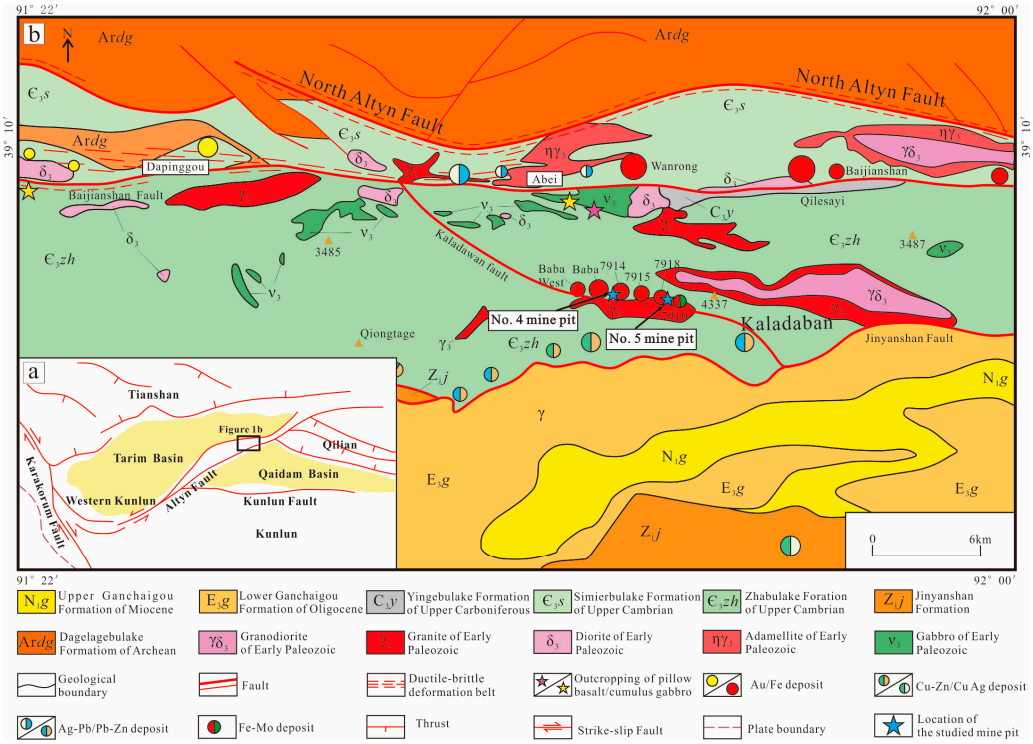

Figure 1. (**a**) Tectonic map of the Altyn Tagh and its adjacent area, modified after [19]. (**b**) Map of regional geology and mineral deposits in the Kaladawan district in the North Altyn Tagh, modified after [3].

The Kaladawan Polymetallic Metallogenic Belt is situated within the North Altyn polymetallic metallogenic subzone, occupying a regional tectonic position from the northern margin of the North Altyn fault zone, to the south of the Lapeiquan–Baijianshan fault and to the north of the Jinyanshan fault (Figure 1b). It encompasses various deposits, including the Kaladaban lead–zinc deposit, Kaladawan West lead–zinc deposit, Kaladawan iron deposit, Wanrong iron deposit, Abei silver–lead deposit, Baijianshan iron deposit, and others. The Kaladawan iron deposit is located in the central and southern parts of the Kaladawan metallogenic belt. Within the mining area, ore bodies are primarily distributed near the contact boundary between marble and basalt in section two of the Lapeiquan Formation (Figure 1b), which is controlled by stratigraphic horizons [18,20].

3. Samples

The studied iron orebody is located in Nanchagou, the Kaladawan iron deposit belt. The exposed strata are relatively intact, primarily consisting of basalt, dacite, marble, mica quartz schist, quartzite, and phyllite. The iron ore is classified as magnetite–specularite type. Basalt is extensively distributed and exhibits an aphanitic texture and massive structures, along with banded, stratiform-like, and pillow structures. The iron orebody stretches from east to west within the contact zone of marble and basalt, exhibiting characteristics of stratification. Two profiles of mine pits No. 5 and No. 4 (Figure 2a,b) were conducted in this study, which correspond to the 7918 and 7914 deposits, respectively (Figure 1). The geographical coordinates of the No. 4 mine pit is a latitude of N 39°05.267′ and a longitude of E 91°44.646′.

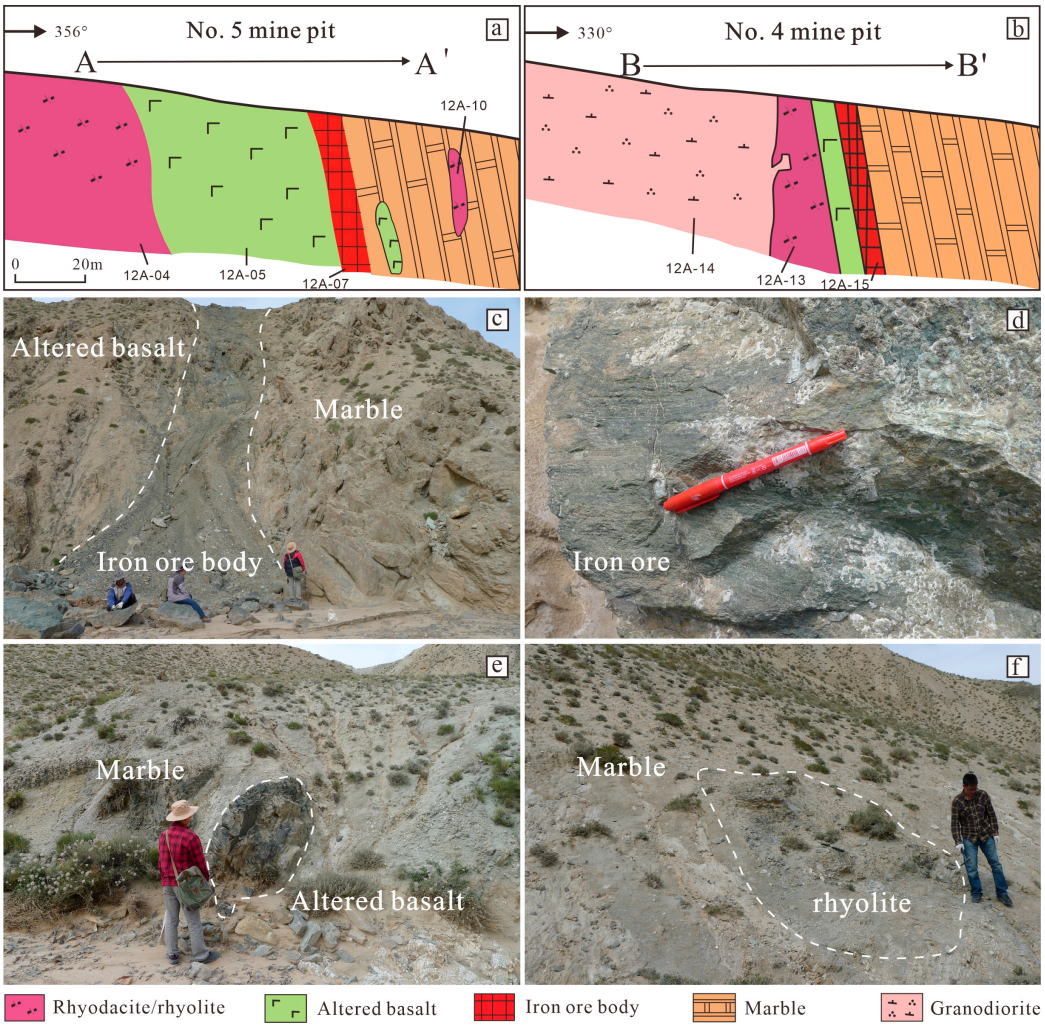

Figure 2. The profile of No. 5 (**a**) and No. 4 (**b**) mine pit and field outcrops (**c**–**f**) of the iron ores, basalt, marble, and rhyolite in the Kaladawan iron deposit.

3.1. No. 5 Mine Pit

The lithological association of the No. 5 mine pit profile from the south to north comprises rhyodacite, altered basalts, iron ore, and marble (Figure 2a), respectively. The iron orebody is located at the contact site between the altered basalts and marble (Figure 2c) with a banded structure (Figure 2d). Basalt and rhyolite lenses were also identified in the marble (Figure 2a,e,f). Samples of rhyodacite (12A-04), altered basalts (12A-05), iron ore (12A-07), and rhyolite in the marble (12A-10) were collected sequentially from the south to the north in this section (Figure 2a).

3.2. No. 4 Mine Pit

The rock type of the No. 4 mine pit profile is similar to that of the No. 5 mine pit, but with the southernmost section consisting of one set granodiorite intrusion, while dacite occurs towards the north (Figure 2b). The iron ore body also occurs at the contact zone between the altered basalt and marble (Figure 2b). Granodiorite (12A-14), rhyodacite (12A-13), and iron ore (12A-15) samples were successively collected from the south to the north in this section as well.

Petrographic studies and geochemical analysis were conducted accordingly.

4. Petrography and Mineralogy

4.1. Rhyodacite/Rhyolite

The rhyodacite (12A-04 and 12A-13) in the No. 5 and No. 4 mine pits both exhibit a porphyritic texture, characterized by predominantly plagioclase phenocrysts with a few quartz ones. The plagioclase phenocrysts are predominantly altered by argillization (Figure 3a) and epidotization (Figure 3b). The matrix is composed of microcrystalline feldspar and quartz with little opaque magnetite, which are arranged around the phenocryst with a rhyolitic structure (Figure 3a,b).

The rhyolite (12A-10) included in the marble shows a porphyritic texture with plagioclase and quartz phenocrysts (Figure 3c), or a spherulitic texture with fibrous feldspar and quartz (Figure 3d). The matrix is composed of magnetite, feldspar, and quartz, exhibiting a felsitic texture (Figure 3c,d).

The grains of magnetite in rhyodacite exhibit a euhedral–subhedral morphology. In some domains, pyrite occurs in a relic shape in the core and in an annular shape in the rim of the magnetite, showing evidence of alteration and oxidation of the pyrite (Figure 3e).

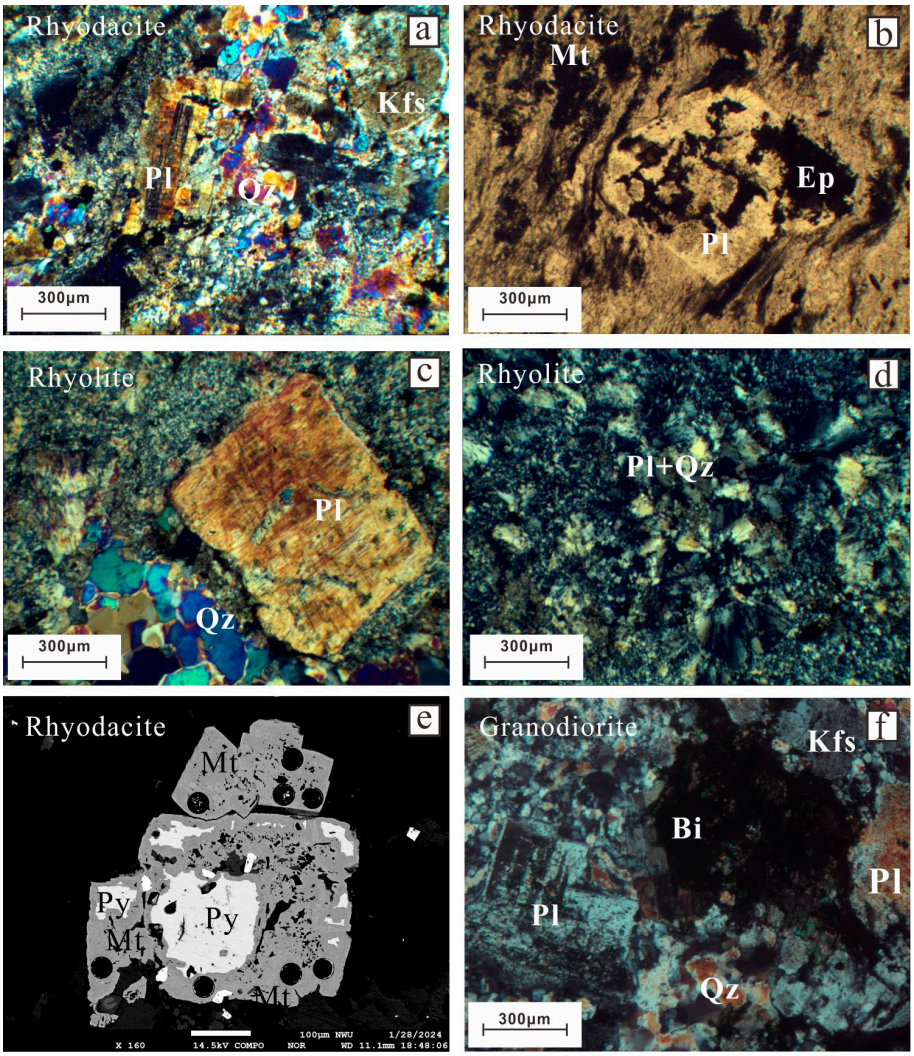

Figure 3. *Cont.*

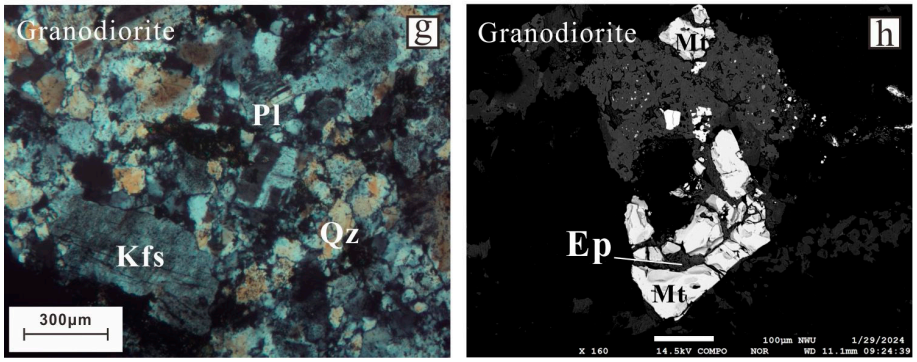

Figure 3. Microscopic photos and BSE images of magnetite of rhyodacite, rhyolite, and granodiorite in the Kaladawan iron deposit. (**a**–**c**) Plagioclase and quartz phenocrysts in rhyodacite/rhyolite. (**d**) Spherulitic texture with fibrous feldspar and quartz. (**e**) Pyrite is altered into magnetite. (**f**,**g**) Plagioclase, quartz, potassium feldspar, and biotite grains in the granodiorite. (**h**) Euhedral magnetite is eroded. Qz, quartz; Pl, plagioclase; Mt, magnetite; Ep, epidote; Kfs, potassium feldspar; Bi, biotite; Py, pyrite.

4.2. Granodiorite

The granodiorite sample (12A-14) is mainly composed of plagioclase, quartz, potassium feldspar, biotite, and minor hornblende and has undergone slight alteration (Figure 3f,g). Magnetite in the granodiorite exhibits a euhedral edge, but with obvious dissolution and numerous fractures filled with epidote and chlorite (Figure 3h).

4.3. Altered Basalt

The altered basalt (12A-05) has been subjected to alteration. The amphibole rim is predominantly chloritized (Figure 4a). Ilmenite and magnetite mostly occur as tiny and euhedral grains distributed in the matrix (Figure 4b,c). In the individual larger grains (>100 μm), the ilmenite is replaced by hematite and rutile (Figure 4d) through the oxidation reaction $4FeTiO_3 + O_2 \rightarrow 2Fe_2O_3 + 4TiO_2$.

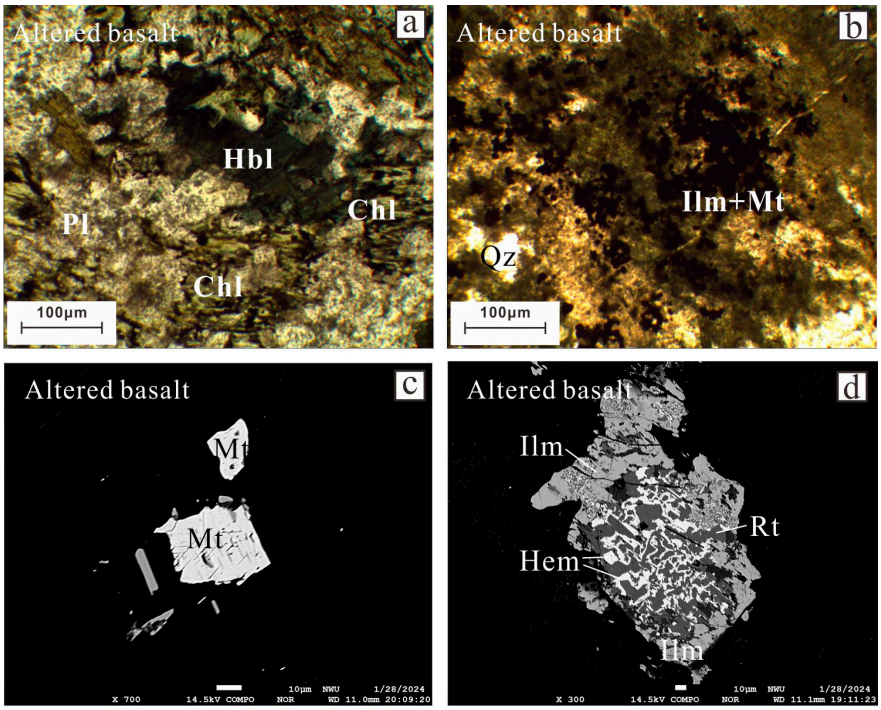

Figure 4. *Cont.*

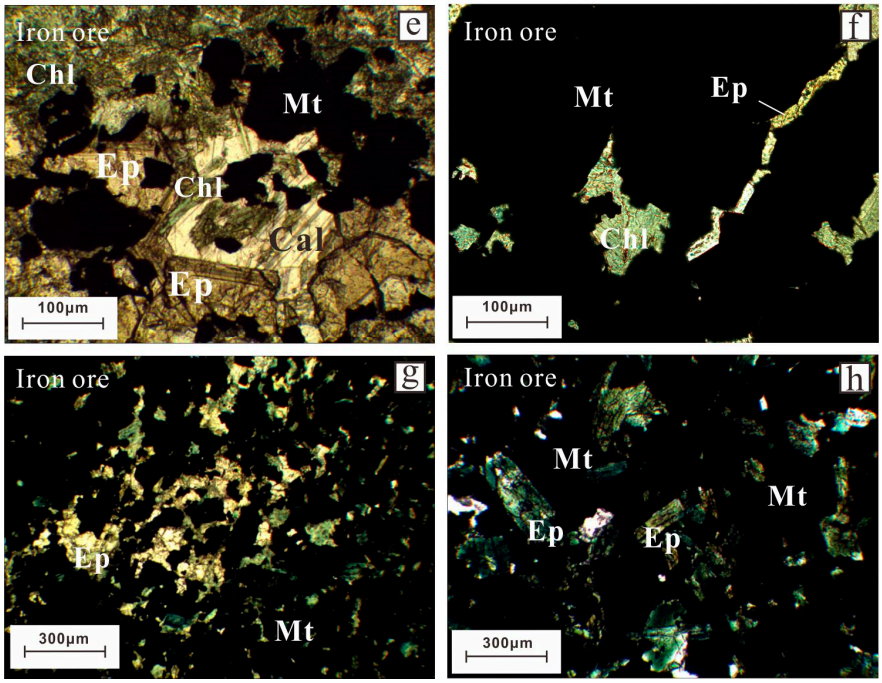

Figure 4. Microscopic photos and BSE images of magnetite in altered basalt and iron ore in the Kaladawan iron deposit. (**a**) Chloritization of hornblende in altered basalt. (**b**) Magnetite and ilmenite occur as tiny grains distributed in the matrix. (**c**) Euhedral–subhedral magnetite grains in altered basalt. (**d**) Ilmenite is oxidized and decomposed into hematite (light) and rutile (dark). (**e**) Chlorite, euhedral epidote, and calcite in the iron ore. (**f**–**h**) Magnetite occurs together with epidote and chlorite. Pl, plagioclase; Chl, chlorite; Mt, magnetite; Ep, epidote; Hbl, hornblende; Cal, calcite; Ilm, ilmenite; Hem, hematite; Rt, rutile.

4.4. Iron Ore

The iron ore exhibits diverse textures, primarily characterized by banded and disseminated structures. Epidote, calcite, and chlorite are the main non-metallic minerals found in the iron ore (Figure 4e–h). The epidote shows a euhedral to subhedral shape and is partially chloritized in the rims (Figure 4e,h). The magnetite in the iron ore is maldistributed, and the mean content is up to 70% (Figure 4e–h). Magnetite also appears to have a euhedral-to-subhedral shape, and it coexists with epidote and chlorite (Figure 4e–h).

5. Analytical Methods

5.1. Whole-Rock Chemistry Analyses

The whole-rock major and trace element analysis was carried out in State Key Laboratory of Continental Dynamics, Northwest University, Xi'an. All pressed samples were tested using an RIX2100 X-ray fluorescence spectrometer with an analytical precision of ±2%. The adopted standards were BCR-2 and GBW07105. Trace element analyses were performed using an Elan 6100DRC plasma mass spectrometer (ICP-MS); standards AGV-1, BCR-1, and BHVO-1 were used for calibration, with an analytical precision of about 0.1 μg/g for lower concentration elements. The analytical accuracy of Co, Ni, Zn, Ga, Rb, Y, Zr, Nb, Hf, Ta, and REEs (except Hf and Lu) was better than 5%, and the analytical accuracy of other elements was better than 5%–10%.

5.2. Magnetite Trace Element Analyses

The trace elements analyses of magnetite were conducted in the thin sections, using an Anglient 7900 ICP MS coupled with a GeoLasHD system in Shandong Provincial Key Laboratory of Depositional Mineralization and Sedimentary Minerals, Shandong University of Science and Technology. A He stream was used to transport aerosol into ICP–MS, where

masses were analyzed. The samples were analyzed through the ablation of a single spot with 44 μm. NIST610 served as the external standard. The BIR-1G, BHVO-2G, and MAKR-NP standards were used for multi-standard calibration, and no internal standard was used. The raw data were processed using ICPMSDataCal [21].

5.3. Fe Isotope Analyses

The Fe isotope test was performed using a multicollector inductively coupled plasma–mass spectrometry (MC-ICP-MS) manufactured by Thermo Fisher Scientific in Waltham, MA, USA. The sample was dissolved in a mixed solution of HF and HNO_3. After drying, the sample was dissolved in nitric acid to oxidize iron to Fe^{3+} completely. Ion exchange chromatography was used to separate Fe from other elements effectively. Mass fractionation was calibrated through the standard sample cross method. The results of Fe isotope analysis are expressed as per thousand deviations relative to the international standard material IRMM-014 [22], where

$$\delta^{56}Fe_{IRMM-014} = \left[\left({}^{56}Fe/{}^{54}Fe \right)_{sample} / \left({}^{56}Fe/{}^{54}Fe \right)_{IRMM-014} - 1 \right] \times 1000$$
$$\delta^{57}Fe_{IRMM-014} = \left[\left({}^{57}Fe/{}^{54}Fe \right)_{sample} / \left({}^{57}Fe/{}^{54}Fe \right)_{IRMM-014} - 1 \right] \times 1000$$

6. Results

6.1. Whole-Rock Chemistry

The major and trace elements of rhyodacite/rhyolite, altered basalts, and iron ores in the Kaladawan iron deposit were analyzed. The results are provided in Supplementary Materials Table S1.

6.1.1. Rhyodacite/Rhyolite

The experimental results revealed the major oxide composition of rhyodacite samples (12A-04) and (12A-13), as well as the rhyolite sample (12A-10), as follows: SiO_2 = 73.90~78.27 wt.%, Al_2O_3 = 11.86~13.98 wt.%, MgO = 0.21~0.59 wt.%, $Mg^{\#}$($Mg^{\#}$ = 100 × $Mg^{2+}/(Mg^{2+} + Fe^{2+})$) = 19.98~59.40, K_2O = 0.07~2.94 wt.%, Na_2O = 5.06~7.46 wt.%, and K_2O/Na_2O = 0.01~0.58 (Supplementary Table S1).

In the ($Na_2O + K_2O$)-SiO_2 diagram (Figure 5a), all three samples are located in the field of rhyolites. The content of $Na_2O + K_2O$ ranges from 6.39 to 8.43 wt.%, and the Rittman index (σ) varies between 1.16 and 2.27 (Supplementary Table S1), suggesting a calc–alkaline series. Moreover, the Aluminum Saturation Index (A/CNK) is in the range from 0.79 to 1.10. In the A/NK-A/CNK diagram (Figure 5b), it is worth noting that rhyodacite (12A-04) samples are located within the peraluminous region, rhyodacite samples (12A-13) are in the metaluminous region, and rhyolite samples (12A-10) are located within the metaluminous–peraluminous region.

In the chondrite-normalized rare-earth element pattern diagram for the rhyodacite/rhyolites (Figure 6a), a pronounced differentiation in rare-earth elements can be observed. The ratio of $(La/Yb)_N$ ranges from 3.30 to 22.59, indicating a relative enrichment of light rare-earth elements (LREEs) and depletion of heavy rare-earth elements (HREEs). Additionally, an obvious negative Eu anomaly (δEu) ranging from 0.20 to 0.32 is displayed. The ratios of $(La/Sm)_N$ range from 2.88 to 7.59, and those of $(Gd/Yb)_N$ range from 0.93 to 1.50 (Supplementary Table S1), suggesting evident internal fractionation of LREE with no internal fractionation of HREE. In the primitive mantle-normalized trace-element diagram (Figure 6b), the three rocks exhibit enrichment in HFSE (e.g., Th, U, Zr, and Hf) and LILE (e.g., La and Ce), while being strongly depleted in K, Sr, P, and Ti.

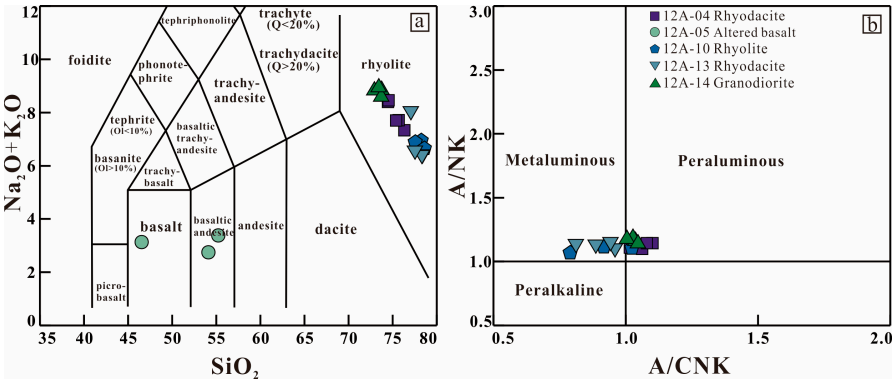

Figure 5. Major elements discrimination diagrams for the rhyodacite/rhyolite, altered basalt, and granodiorite in the Kaladawan area: (**a**) (Na_2O + K_2O)-SiO_2 (modified after [23]) and (**b**) A/NK-A/CNK diagrams (modified after [24]).

6.1.2. Altered Basalt

The altered basalt samples (12A-05) show a variation in compositions: SiO_2 = 46.75~55.40 wt.%, Al_2O_3 = 12.99~15.71 wt.%, TFe_2O_3 = 9.75~15.92 wt.%, MgO = 6.15~7.58 wt.%, TiO_2 = 0.71~1.01 wt.%, CaO = 4.86~8.04 wt.%, Na_2O = 2.16~2.46 wt.%, and Na_2O + K_2O = 2.80~3.42 wt.% (Supplementary Table S1). The $Mg^{\#}$ ranges from 52.60 to59.51, which is lower than the primary basalt $Mg^{\#}$ of 70 [25]. In the (Na_2O + K_2O)-SiO_2 diagram, the altered basalt samples fall within the basalt and basaltic andesite field (Figure 5a).

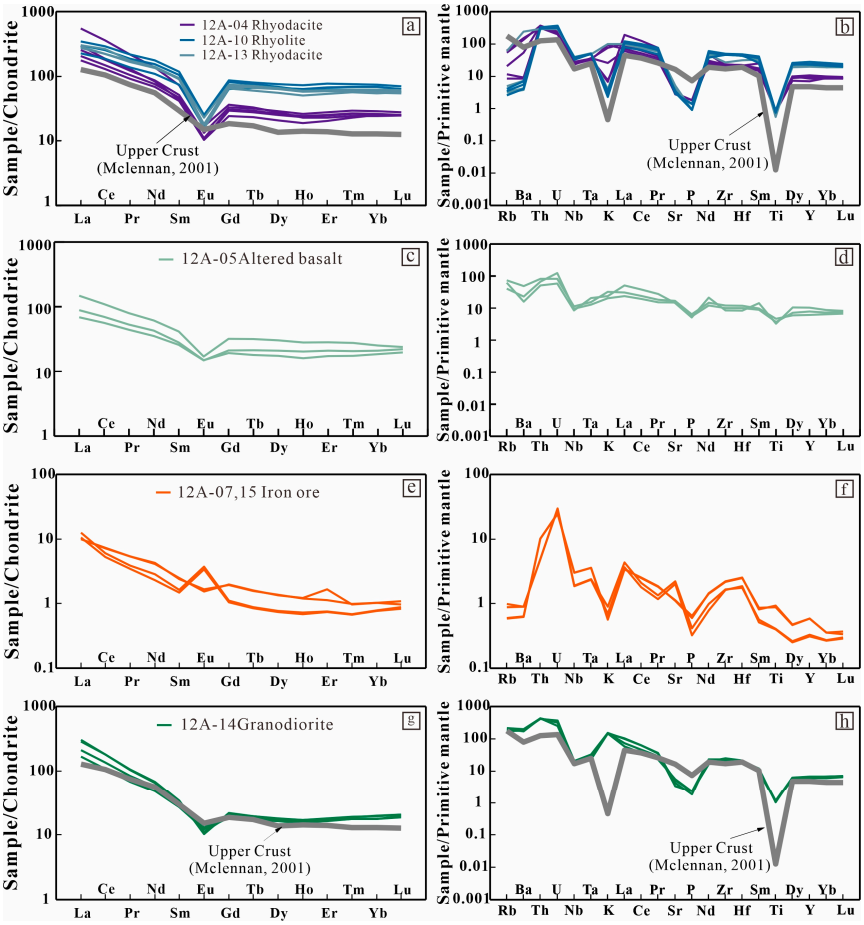

Figure 6. Chondrite-normalized REE patterns (**a**,**c**,**e**,**g**) and primitive mantle-normalized trace-element spider diagrams (**b**,**d**,**f**,**h**) of rhyodacite/rhyolite, altered basalt, granodiorite, and iron ore in the Kaladawan area. Normalization after Sun and McDonough [26]; the upper crust data are from [27].

The chondrite-normalized rare-earth element pattern diagram of the altered basalt (Figure 6c) indicates unobvious differentiation of LREE and HREE, with the $(La/Yb)_N$ ranging from 3.3 to 5.9 (Supplementary Table S1). In the primitive mantle-normalized trace-element diagram (Figure 6d), HFSE (e.g., Th, U, Zr, and Hf) and LILE (e.g., La and Ce) are enriched, while Ba, P, and Ti are depleted.

6.1.3. Iron Ore

The two samples (12A-07) and (12A-15) of Kaladawan iron ore have TFe_2O_3 content ranging from 73.34 to 80.44 wt.%, SiO_2 content ranging from 11.03 to 13.61 wt.%, MgO content ranging from 2.5 to 3.31 wt.%, and CaO content ranging from 4.08 to 7.1 wt.% (Supplementary Table S1).

The chondrite-normalized rare-earth element pattern diagram for the iron ore samples (Figure 6e) exhibits a right-leaning LREE enrichment pattern, with $(La/Yb)_N$ values varying between 9.57 and 15.95. The ΣREE ranges between 8.29 and 11.06 ppm (Supplementary Table S1), which is significantly lower when compared to those of the rhyodacite/rhyolites and altered basalt. Furthermore, the primitive mantle-normalized trace-element diagram (Figure 6f) exhibits an enrichment of HFSE (e.g., Th, U, Zr, and Hf), as well as LREE (e.g., La and Ce).

6.1.4. Granodiorite

The compositions of granodiorite (12A-14) are as follows: SiO_2 = 72.52~73.47 wt.%, MgO = 0.27~0.35 wt.%, Al_2O_3 = 13.65~14.06 wt.%, TFe_2O_3 = 2.17~2.41 wt.%, $Mg^{\#}$ = 22.48~25.31, and $Na_2O + K_2O$ = 8.56~8.86 wt.%. The Rittman index(σ) is 2.40~2.64 (Supplementary Table S1), indicating a calcium alkaline series. In the $(Na_2O + K_2O)$-SiO_2 diagram (Figure 5a), the sample falls into the rhyolite category and shows a sub-alkaline series; in the A/NK-A/CNK diagram, it is shown as a peraluminous rock (Figure 5b).

The chondrite-normalized rare-earth element patterns diagram (Figure 6g) exhibits a right-leaning LREE enrichment and relative HREE depletion pattern, with $(La/Yb)_N$ ranging from 9.46 to 17.13, and a negative Eu anomaly with δEu ranging from 0.37 to 0.54. On the primitive mantle-normalized trace-element diagram (Figure 6h), the sample is enriched in Rb, Ba, K, and significant LILE while being strongly depleted in P and Ti. This trend is generally consistent with that observed for rhyolite.

6.2. Fe Isotope

Three samples of altered basalts (12A-05), four samples of iron ore (12A-07) and (12A-15), three samples of rhyodacite (12A-04), and three samples of granodiorite (12A-14) were selected for whole-rock isotope determination. The results of the Fe isotope test are shown in Table 1.

Table 1. Fe isotope analysis results of whole-rock samples of altered basalt, iron ore, rhyodacite, and granodiorite in Kaladawan area; SK basalt from [9].

Sample	Description	TFe_2O_3 (wt.%)	TFe_2O_3/TiO_2	$\delta^{56}Fe$ (‰)	2SD	$\delta^{57}Fe$	2SD	F
SK-01	Weakly altered basalt	15.00	27.27	0.129	0.041	0.201	0.063	0.37
SK-02	Unaltered basalt	16.90	73.48	0.197	0.041	0.301	0.063	
12A-05	Altered basalt	9.75	9.65	0.100	0.033	0.141	0.054	0.13
		15.92	22.42	0.082	0.032	0.091	0.053	0.31
		11.72	14.65	0.024	0.031	0.023	0.050	0.20
12A-07	Iron ore	80.44		0.171	0.017	0.264	0.029	
		80.03		0.142	0.014	0.205	0.028	
12A-15		73.66		0.152	0.018	0.235	0.028	
		73.34		0.062	0.023	0.092	0.035	

Table 1. *Cont.*

Sample	Description	TFe_2O_3 (wt.%)	TFe_2O_3/TiO_2	$\delta^{56}Fe$ (‰)	2SD	$\delta^{57}Fe$	2SD	F
12A-04	Rhyodacite	1.96		0.120	0.014	0.191	0.028	
		1.91		0.212	0.015	0.301	0.026	
		2.00		0.245	0.020	0.336	0.030	
12A-14	Granodiorite	2.41		0.224	0.023	0.319	0.041	
		2.27		0.128	0.035	0.177	0.060	
		2.35		0.108	0.018	0.150	0.028	

The $\delta^{56}Fe$ values for the three altered basalt samples are 0.024‰–0.100‰, with an average of 0.069‰. The $\delta^{56}Fe$ values for the four iron ore samples are 0.062‰–0.171‰, with an average of 0.132‰. The $\delta^{56}Fe$ values for the three rhyodacite samples are 0.120‰–0.245‰, with an average of 0.193‰. The three granodiorite samples have $\delta^{56}Fe$ = 0.108‰–0.224‰, with an average of 0.153‰.

6.3. Magnetite Chemistry

The chemical compositions of trace elements in magnetite from rhyodacite, altered basalt, iron ore, and granodiorite are presented in Supplementary Table S2.

6.3.1. Rhyodacite

The concentrations of rare-earth elements in rhyodacite are generally low, ranging from ΣREE = 0.054 to 892.2 ppm, Zr = 0.032 to 206.2 ppm, Cr = 0.00 to 20.22 ppm, Mg = 2707 to 4988 ppm, and V = 0.195 to 3.170 ppm (Supplementary Table S2). The multi-element pattern diagram illustrates a significant enrichment of Pb, Mo, and Co in rhyodacite magnetite, while showing depletion in Zr, Nb, Ti, and V (Figure 7a).

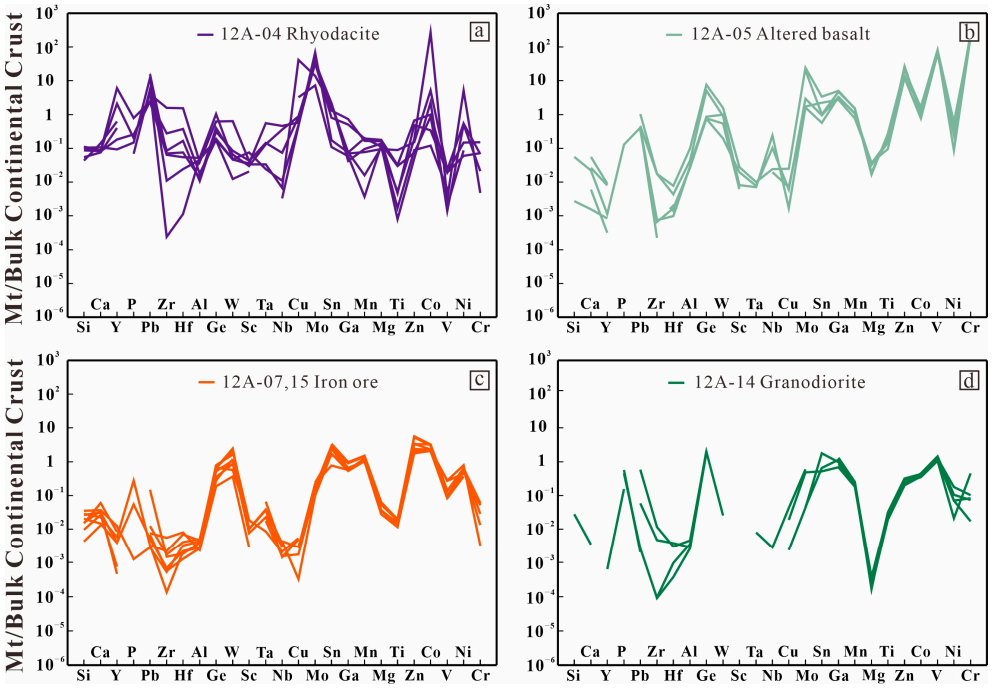

Figure 7. Multi-element pattern diagram of magnetite from rhyodacite (**a**), altered basalt (**b**), iron ore (**c**), and granodiorite (**d**) in the Kaladawan iron deposit (normalized to the bulk continental crust; data from [28]).

6.3.2. Altered Basalt

The magnetite in altered basalts exhibits ΣREE values ranging from 0.050 to 3.401 ppm, with heavy rare-earth elements generally below the detection limit. Zn concentrations range from 874.3 to 1939 ppm, V ranges from 8635 to 11,193 ppm, and Cr ranges from 26,114 to 34,063 ppm (Supplementary Table S2). The multi-element pattern diagram reveals a strong enrichment of Ge, Ga, Mo, Zn, V, and Cr in the altered basalt magnetite, while exhibiting significant depletion of Y, Zr, Hf, and Cu (Figure 7b).

6.3.3. Iron Ore

The concentration of rare-earth elements (ΣREEs) in iron ore magnetite is relatively low, ranging from 0.106 to 1.136 ppm, with heavy rare-earth elements generally exhibiting lower values than the detected levels; V ranges from 11.37 to 37.82 ppm, while Cr varies between 0.00 and 8.031 ppm (Supplementary Table S2). The multi-element pattern diagram illustrates a strong enrichment of Ge, W, Sn, Mn, Zn, and Co in iron ore magnetite and a depletion of Y, Zr, Hf, Nb, and Cu (Figure 7c).

6.3.4. Granodiorite

The concentration of most trace elements of magnetite in granodiorite falls below the detection limit of the instrument, with ΣREE ranging from 0.021 to 1.080 ppm, Ge ranging from 2.462 to 2.730 ppm, V ranging from 146.6 to 197.2 ppm, and Cr ranging from 2.296 to 61.04 ppm (Supplementary Table S2). The multi-element pattern diagram reveals a significant enrichment of Ge, Sn, Ga, and V in magnetite, while showing depletion in Zr and Mg (Figure 7d).

7. Discussion

7.1. Genesis of the Iron Deposit

The genesis of the Kaladawan iron deposit remains a subject of controversy, due to its intricate history involving multiple stages of magmatism. At present, there exist several predominant viewpoints regarding the origin of this deposit: (1) Formation through volcanic sedimentation followed by skarnization [3,7–9]; (2) SVIO hypothesis [5]; (3) Skarn-type formation [10]. Skarn-type deposits form in or near the contact zone between intermediate–acid and intermediate–basic magmatite and carbonate rocks, resulting from the metasomatism of the surrounding rocks by magmatic hydrothermal fluids. Within these fluid systems, magnetite serves as the primary mineral phase for precipitation [29]. The composition and texture of magnetite can be influenced by variations in physicochemical parameters such as temperature, oxygen fugacity, and melt composition of the magmatic–hydrothermal fluids [30].

The Ni/Cr ratios of hydrothermal magnetite typically exhibit values greater than or equal to 1 [31]. In the case of Kaladawan iron ore samples (12A-07, 15), their Ni/Cr ratios range from 3.979 to 107.8, surpassing the threshold of 1 overall. These samples are distributed within the region corresponding to hydrothermal magnetite on a (Ni/Cr)-Ti diagram (Figure 8a). However, magnetite is prone to textural and compositional re-equilibration, which can lead to a significantly different geochemical model compared to the previous one. Therefore, caution should be exercised when utilizing the Ti-(Ni/Cr) diagram [30,32–34]. Previous studies have proposed a more effective Fe-(V/Ti) diagram for distinguishing between magmatic and hydrothermal magnetite. This diagram comprises three distinct regions: magmatic magnetite, re-equilibrated magnetite, and hydrothermal magnetite (Figure 8b). Magmatic magnetite typically exhibits V/Ti values < 1 and Fe content < 66%, while hydrothermal magnetite generally displays V/Ti values > 1 [30]. In the Fe-(V/Ti) diagram, magnetite in the studied iron ore falls into the hydrothermal magnetite area; however, the magnetite derived from altered basalt and rhyodacite samples are situated in the re-equilibrated region (Figure 8b). The primary mechanism responsible for this re-equilibration in igneous rocks is fluid-induced dissolution–reprecipitation [30]. It is worth noting that the formation of magnetite in altered basalt and rhyodacite might

have been influenced by the magmatic hydrothermal fluids; for example, the pyrite in the rhyodacite was replaced by magnetite (Figure 3e) and the ilmenite in the altered basalt underwent oxidative decomposition to rutile and hematite (Figure 4d), suggesting that hydrothermal metasomatism has played a role in the formation process.

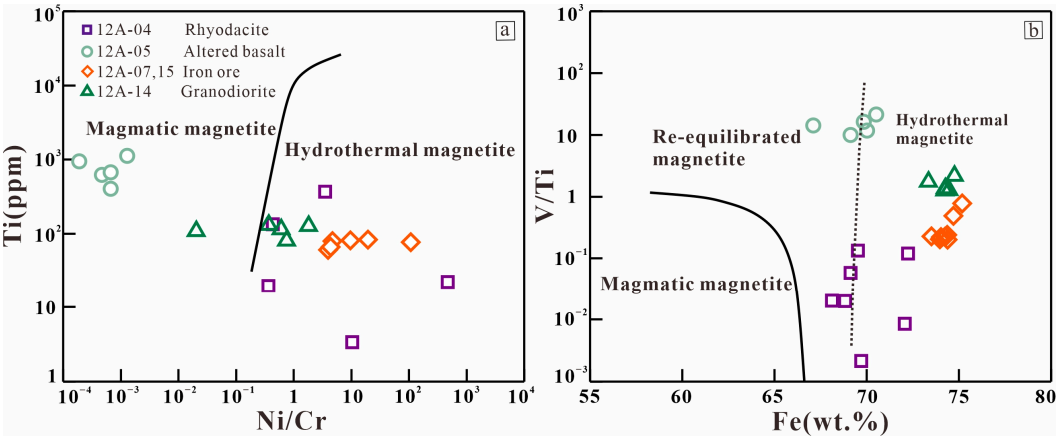

Figure 8. The genesis diagram of magnetite in different rocks from the Kaladawan iron deposit: (**a**) Ti-(Ni/Cr) (modified from [31]) and (**b**) (V/Ti)-Fe (modified from [30]).

The (Ca + Al + Mn)-(Ti + V) and (Ni/(Cr + Mn))-(Ti + V) diagrams have been proven to be effective in distinguishing various types of deposits, including iron oxide–copper–gold (IOCG), Kiruna, porphyry Cu, banded iron formation (BIF), Fe–Ti–V, and skarn deposits [35]. In these diagrams (Figure 9), magnetite from the iron ore consistently falls within the skarn area. In addition, hydrothermal magnetite exhibits high Si, Ca, and Mg content, but low Ti, Al, Cr, and Ni levels [31]. In the multi-element variation diagram, the magnetite in the Kaladawan iron ore exhibits characteristics of high Si, Ca, Ge, and Mo content and low Ti, Al, and Cr levels, as depicted in Figure 10. These findings are consistent with those documented for the Kaladawan magnetite sample [36] and the typical skarn iron deposits [31,37].

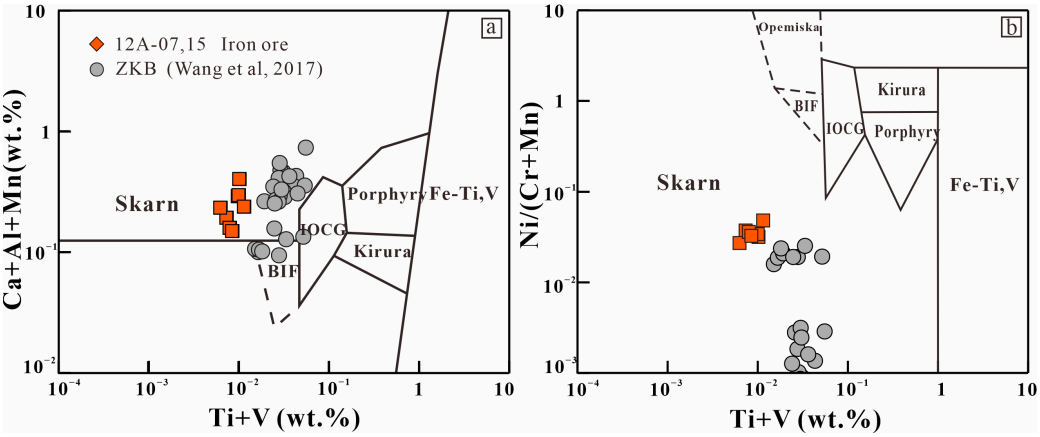

Figure 9. Discrimination diagram for magnetite from the iron ore in the Kaladawan iron deposit: (**a**) (Ca + Al + Mn)-(Ti + V) and (**b**) (Ni/(Cr + Mn))-(Ti + V), modified after [35]. ZKB data are from [36].

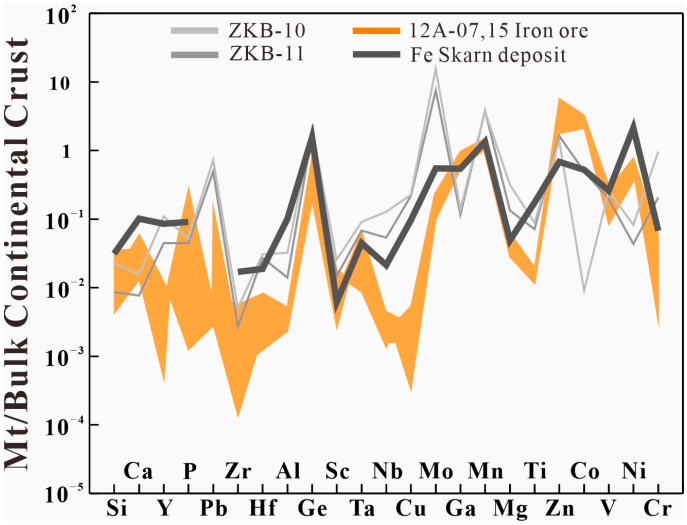

Figure 10. Multi-element diagram of magnetite normalized to the bulk continental crust, the data are from [28], the Fe Skarn deposit data are from [31], and the ZKB-10 and ZKB-11 data are from [36].

Additionally, Fe isotope analysis can effectively discriminate between different deposit types [38–40]. The measured samples from the Kaladawan iron deposit all exhibit positive Fe isotopes, ranging from δ^{56}Fe 0.024 to 0.245‰; this distribution significantly deviates from that observed in low-temperature hydrothermal and magmatic iron deposits (Figure 11), but it aligns with the range seen in three other typical skarn iron deposits found in China, thus confirming a close association between the Kaladawan iron deposit and skarn-type deposits.

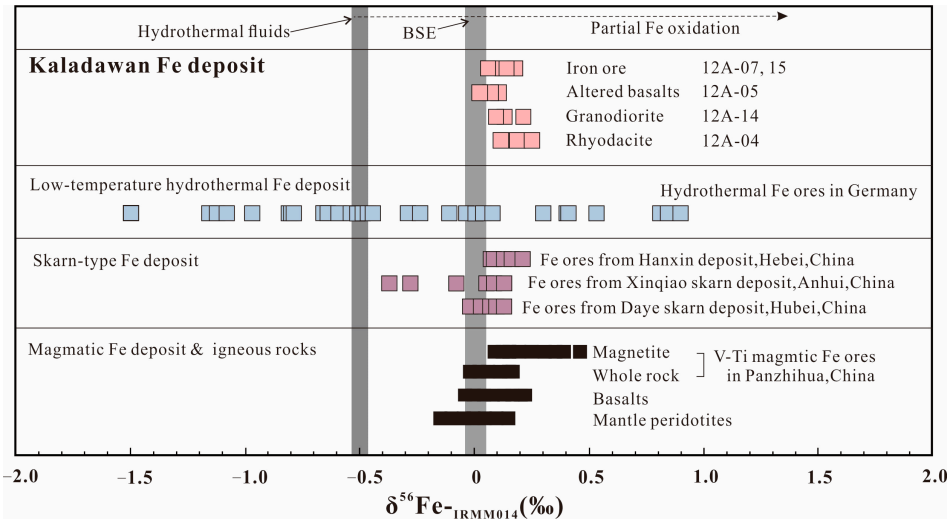

Figure 11. The Fe isotope composition of the four rocks from the Kaladawan iron deposit and other iron deposits worldwide (modified after [41]). BSE, Bulk Silicate Earth.

In summary, the Kaladawan iron ore body is situated within the contact zone between the basalt and marble (Figure 2c) and mainly consists of hydrous minerals, such as epidote and chlorite, showing the typical characteristics of skarn-type iron deposit (Figure 4e–h). Moreover, the Ti-(Ni/Cr) and (V/Ti)-Fe diagrams indicating the hydrothermal genesis of magnetite (Figure 8), the skarn-type deposit location within the (Ca + Al + Mn)-(Ti + V) and (Ni/(Cr + Mn))-(Ti + V) diagrams (Figure 9), and the Fe isotope characteristics collectively validate that the Kaladawan iron deposit can be classified as skarn-type.

7.2. Source of Ore-Forming Material

The behavior of REE and fractionation of Fe isotopes during mineralization were discussed extensively. Determining the origin of metal elements is a fundamental issue in ore formation that can be addressed through the use of various geochemical methods. Rare-earth elements, due to the fact that they are almost inert in nature and have similar geochemical properties, serve as valuable tracers for identifying the source of ore-forming materials throughout the mineralization process. Through analyzing the compositional features and distribution patterns of rare-earth elements in different rocks, along with assessing ore-forming environments and physicochemical conditions, it becomes possible to effectively explain the source of ore-forming materials, ore formation conditions, and ore-forming fluids [42–44].

The ΣREE content of iron ore from Daye, Altay Wutubulak, and Mengku—which are characterized by typical skarn genesis—is notably lower compared to that in skarn deposits; however, the REE distribution patterns between iron ore and skarn exhibit consistency [45,46]. The total amount of rare-earth elements present in the iron ores within this study ranged from 8.29 to 11.06 ppm, which is lower compared to the altered basalts (95.85~172.98 ppm). Additionally, the LREE/HREE ratios range from 7.05 to 11.16 for iron ores versus 3.88~5.56 for altered basalts; furthermore, the $(La/Yb)_N$ values are in the range of 9.57~15.95 for the iron ores, versus 3.30~5.90 for the altered basalts. Moreover, the REE distribution pattern exhibited by the altered basalts and iron ores demonstrates a consistent right-leaning pattern with enrichment of light rare-earth elements. These findings suggest that the iron ores inherited the specific REE characteristics from their associated altered basalts, which is consistent with inheritance characteristics observed previously in skarn-associated iron ores (Figure 12a).

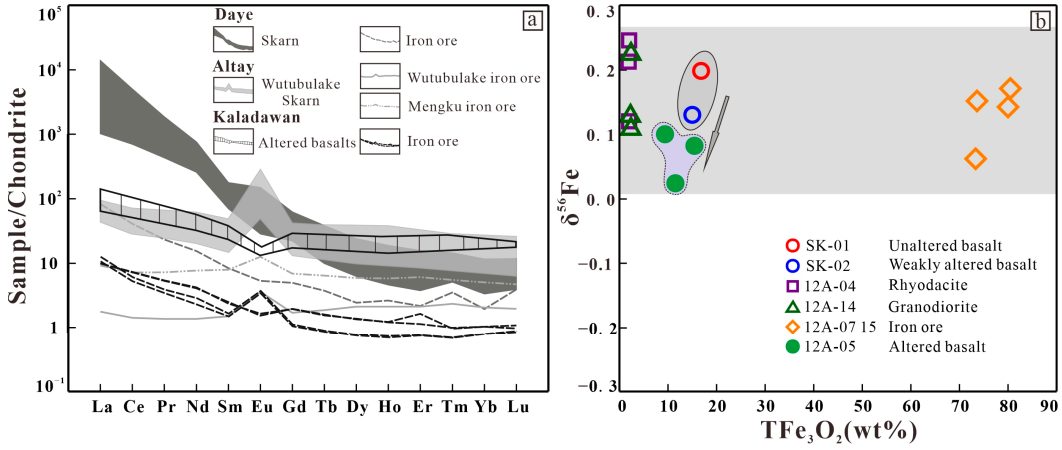

Figure 12. (**a**) The chondrite-normalized REE patterns diagram of altered basalt, iron ore, and typical skarn iron ore in the Kaladawan iron deposit. Data of Daye, Altay Wtubulak, and Mengku iron ores are from [45,46], and standardized values are from [26]. (**b**) δ^{56}Fe-TFe_3O_2 variation relationship between the rhyodacite/rhyolite, granodiorite, iron ore, altered basalt, and unaltered basalt. The Fe isotope data of SK basalts are from [9]. The gray area indicates the range of Fe isotope values from the studied samples.

Although rare-earth elements (REEs) can indicate the source of ore-forming materials, they do not directly constrain the presence of ore-forming metals. Therefore, this study utilized iron isotopes to trace the origin of these materials. In general, marble exhibits a low total iron content. Furthermore, previous research has demonstrated that skarn-type iron deposits primarily derive their iron from a single igneous rock source, with minimal contributions from other sources [47]. Thus, analyzing the Fe isotopic compositions in igneous rocks within this mining area provides further insights into the origin of ore-forming materials.

The magnetite identified in rhyodacite/rhyolite, altered basalt, and iron ore in this study was shown to originate from hydrothermal genesis (Figure 8), indicating that these rock types underwent hydrothermal impact. Previous studies have documented that magnetite crystals preferentially incorporated heavy Fe isotopes from the ore-forming fluids during the hydrothermal alteration process, attributed to their substantial Fe^{3+} content, which exhibited a higher enrichment of heavy isotopes compared to minerals containing Fe^{2+} [48–50]. Consequently, the hydrothermally altered rock mass exhibits greater enrichment in light iron isotopes, compared to the unaltered rock mass. The altered basalts ($\delta^{56}Fe$ = 0.024‰~0.100‰) exhibited light Fe isotope enrichment, compared to the unaltered basalts ($\delta^{56}Fe$ = 0.129‰~0.197‰; Figure 12b), indicating their potential role as a source of ore-forming materials involved in iron deposit formation. Also, the TFe_2O_3 content in altered basalts, which ranged from 9.75 wt% to 15.92 wt% (Table 1), is lower than that of the unaltered basalts in the same region (TFe_2O_3 = 16.90 wt%; Table 1 and Figure 12b) [9], indicating that the iron ores were formed at the expense of basalts.

Therefore, according to the above studies, the basaltic rock could be an ore-forming material. The dissolution of hydrothermal fluid brings out the heavy iron isotope in basalt, which leads to the low $\delta^{56}Fe$ value of altered basalt, thus providing the main Fe for mineralization.

7.3. The Possible Origin of the Hydrothermal Fluid

It is known that skarn-type iron deposits are closely associated with intermediate-to-acidic igneous rocks. The intrusion of the intermediate–acid magma into carbonate rocks generates hydrothermal fluids that facilitate migration, enrichment, and precipitation processes associated with iron deposition [51]. In this study, the genesis of magnetite and petrography proved that hydrothermal fluid played a role in the formation of iron ore. Based on the rock assemblages in the studied iron ore, the granodiorite may be the sole potential source of hydrothermal fluid.

Firstly, abundant dating data have consistently demonstrated that the intrusive ages of granite or granodiorite range from 476 to 480 Ma [9,10,52] (unpublished data by authors), while the ages of the rhyodacite range from 495 to 506 Ma [unpublished data by authors], and the age of tholeiitic basalt was determined to be 517 Ma [3,9]. Based on these geochronological findings, it can be inferred that the intrusion of granodiorite occurred after the formation of the rhyodacite and basalt. With regards to the mineralization age, the skarn-type mineralization in Kaladawan iron deposit was confirmed to have occurred during 482.6–481.0 Ma based on the dating of garnet (482.6 ± 4.4 Ma) and titanite (481.0 ± 3.9 Ma) within the skarnized volcanic rock [10], consistent with the intrusive age of the granodiorite. Therefore, in terms of temporal considerations, it is suitable.

Secondly, Fe and Ti exhibit similar geochemical properties, making the TFe_2O_3/TiO_2 ratio a reliable indicator of the rock alteration degree. Through the application of the mass conservation theorem, it is possible to calculate the Fe isotope composition separately from the unaltered protolith [53]. Similarly, based on the mass conservation theorem, $\delta^{56}Fe_i \approx \delta^{56}Fe_{altered} \times F + \delta^{56}Fe_{leached} \times (1 - F)$ [9], we estimate that the Fe isotope composition derived from basalt during the alteration process ranges from $\delta^{56}Fe_{leached}$ = 0.211‰~0.249‰. In this equation, $\delta^{56}Fe_i$ represents the isotopic composition of unaltered basalt, $F = (TFe_2O_3/TiO_2)_{altered}/(TFe_2O_3/TiO_2)_i$ denotes the ratio of altered basalt to unaltered basalt in terms of Fe content, and $\delta^{56}Fe_{altered}$ represents different degrees of alteration in basalt samples. Based on these findings, if all iron in an iron ore originates from basalt, its theoretical $\delta^{56}Fe$ should range between 0.211‰ and 0.249‰ (Table 1), which significantly deviates from the iron ore values ($\delta^{56}Fe$ = 0.062‰~0.171‰) observed in this study. This discrepancy suggests that there should be other sources blended in the ore-forming materials in the iron ore, one of which likely possesses the light Fe isotope.

During the hydrothermal alteration process of iron deposits, the natural fractionation of Fe isotopes occurs. The distinct Fe isotope characteristics observed in skarnized rocks, magnetite deposits, and genesis rocks of the deposits can provide valuable insights into their respective iron sources and the fluid exsolution history within them. In the high-temperature magmatic–hydrothermal mineralization process, exsolution fluids are found to be enriched in lighter Fe isotopes, compared to the stock [47]. The Fe carried in the magmatic–hydrothermal fluid of intermediate–acid magmatic rocks exists as $FeCl_2$ [47,54,55]; this fluid is enriched in light isotopes of Fe, while magmatic rocks are enriched in heavy isotopes of Fe [9]. In this study, the iron ore ($\delta^{56}Fe$ = 0.062‰~0.171‰) demonstrates an enrichment of light Fe isotopes relative to granodiorite ($\delta^{56}Fe$ = 0.108‰~0.224‰); meanwhile, the iron ore has an intermediate Fe isotopic composition between the granodiorite and basalt (Figure 12b and Table 1), suggesting that the granodiorite may serve as a potential source of hydrothermal fluid containing light Fe isotope for the formation of iron ore.

Thirdly, as mentioned above, the magnetite derived from altered basalt and rhyodacite is situated in the re-equilibrated region shown in Figure 8b, indicating alteration by the hydrothermal fluids. Petrographic observations reveal that pyrite in rhyodacite underwent oxidation to form magnetite (Figure 3e), while ilmenite in the altered basalt is oxidized and decomposed into hematite and rutile (Figure 4d), further confirming the hydrothermal alteration of rhyodacite and basalt. Moreover, considering its location at the southernmost part of the profile and its separation from the iron ore body by rhyodacite and basalt (Figure 2b), it is plausible to suggest that hydrothermal fluids derived from granodiorite played a significant role.

Therefore, the hydrothermal fluid from the late granodiorite passed through the rhyodacite and basalt, respectively, and eventually metasomatized with marble, contributing to the enrichment of ore-forming elements.

8. Conclusions

(1) Geochemical studies suggest that the magnetite from different types of rocks in the Kaladawan iron ore is formed through hydrothermal metasomatism, indicating that the deposit is of skarn origin.
(2) The consistent distribution pattern of rare earth elements in the altered basalt and iron ore, along the lower content of heavy isotopes of Fe observed in the altered basalt compared to the unaltered basalt, suggests that the basalt plays a significant role as one of the ore-forming materials.
(3) The hydrothermal fluid responsible for the formation of iron ore carrying the light Fe isotope derived from the late intrusive granodiorite.

Supplementary Materials: The following supporting information can be downloaded at: https://www.mdpi.com/article/10.3390/min14060589/s1, Table S1: Result of major and trace elements analyses for the different rock types in the Kaladawan iron ore deposit; Table S2: Trace element of the magnetite from different rock types in the Kaladawan iron ore deposit.

Author Contributions: Conceptualization, methodology, and writing and data curation, Y.C. (Yuyao Chen) and Y.C. (Yuting Cao); project administration, Y.C. (Yuting Cao) and L.L.; resources, Y.C. (Yuting Cao), C.W. and Y.G.; supervision: W.Y., L.S. and F.X.; review and editing, Y.C. (Yuting Cao) and T.X. All authors have read and agreed to the published version of the manuscript.

Funding: This work was supported by funds from the National Natural Science Foundation of China (Grant No. 42172067) and the SDUST Research Fund and the China Geological Survey (Grants Nos. DD20179395, DD20190376).

Data Availability Statement: All the data are presented in the paper.

Acknowledgments: We sincerely appreciate the editors and three reviewers for their constructive comments, which helped to significantly improve the manuscript.

Conflicts of Interest: The authors declare no conflict of interest.

References

1. Chen, B.L.; Jiang, R.B.; Li, L.; Chen, Z.L.; Qi, W.X.; Liu, R.; Cui, L.L.; Wang, S.X. Discovery of iron ore zones in the Kaladawan area within the eastern part of the Altun Mountains and its significance. *Acta Geosci. Sin.* **2009**, *30*, 143–154.
2. Qi, W.X.; Ma, Y.Z.; Wang, R.; Wei, X.C.; Jiang, J.Y. The geological characteristics of Baba iron deposit, northern margin area of Altyn Mountain and its criteria for prospecting and genesis. *Xinjiang Geol.* **2008**, *26*, 253–257.
3. Chen, B.L.; Li, L.; Qi, W.X.; Chen, Z.L.; Wang, Y.; Hao, R.X.; Li, S.B.; Zhou, Y.G.; Jiang, R.B.; Han, F.B.; et al. Geological characteristics and metallogenic age of Kaladawan iron orefield in Altun Mountains, northwestern China. *Miner. Depos.* **2016**, *35*, 315–334.
4. Ni, K. Characteristics and genesis analysis of Kaladawan iron deposit in Ruoqiang county, Xinjiang, NW China. *Acta Mineral. Sin.* **2013**, *33*, 405.
5. Hou, T.; Zhang, Z.C.; Pirajno, F.; Santosh, M.; Encarnacion, J.; Liu, J.L.; Zhao, Z.D.; Zhang, L.J. Geology, tectonic settings and iron ore metallogenesis associated with submarine volcanism in China: An overview. *Ore Geol. Rev.* **2014**, *57*, 498–517. [CrossRef]
6. Guo, H.J. On the analysis of geological characteristics and genesis of Kaladawan area iron mine in Ruoqiang county of Xinjiang province. *Geol. Fujian* **2015**, *34*, 45–51.
7. Hao, R.X. The Characteristics and Genetic of Kaladawan Area Iron Deposit, Altyn Tagh, Xinjiang. Master's Thesis, Chinese Academy of Geological Sciences, Beijing, China, 2013.
8. Pan, C.Z.; Chen, B.L.; Chen, Z.L.; Hao, R.X. The origin of the Kaladawan iron deposit—New evidence from the geochemistry, Altun Tagh Mountains, NW China. *Xinjiang Geol.* **2015**, *33*, 340–346.
9. Meng, L.T. The Characteristics of Ore Controlling Structure for Kaladawan Iron Ore-Field in the North Altun Area, Xinjiang. Master's Thesis, Chinese Academy of Geological Sciences, Beijing, China, 2016.
10. Wang, C.M.; Zhou, M.L.; Zhong, L.F.; Li, D.F. Garnet and titanite U–Pb dating of the Kaladawan Fe–Mo orefield in the Altyn Mountains, NW China: Constrains for ore genesis. *Ore Geol. Rev.* **2022**, *140*, 104575. [CrossRef]
11. Wang, Y.; Wu, Y.; Chen, B.L.; Chen, Z.L.; Wang, B.; Shi, Y.H.; Tan, R.W.; Gao, Y.; Shen, J.H. Geochemical characteristics and metallogenic potential of ultrabasic rocks in North Altun area, Xinjiang. *Geol. China* **2020**, *47*, 1220–1240.
12. Wu, Y.; Chen, Z.L.; Chen, B.L.; Wang, Y.; Meng, L.T.; He, J.T.; Wang, B.; Han, M.M. Geochemistry, zircon SHRIMP U-Pb dating and Hf isotpic compositions of the monzogranite from the southern Kaladawan of North Altyn and their implications for crust-mantle interaction. *Acta Geosci. Sin.* **2017**, *91*, 1227–1244.
13. Che, Z.C.; Liu, L.; Liu, H.F.; Luo, J.H. The discovery of high-pressure metamorphic argillaceous rocks and its occurrence environment in the Altun Mountains, Northwest China. *Chin. Sci. Bull.* **1995**, *40*, 1298–1300.
14. Chen, X.H.; Wang, X.F.; Yang, F.; Chen, Z.L.; Chen, B.L.; Wang, K.Z. Tectonic enviroments of magmatism in Early Paleozoic in the north Altyn Tagh, China. *J. Geomech.* **2001**, *7*, 193–200.
15. Yang, Y.; Chen, X.H.; George, G.; Wang, X.F.; Qin, H.; Chen, Z.L.; Yang, F.; Chen, B.L.; Li, X.Z. Early Paleozoic magmatism and gold metallogenesis in Altun Mountains, Northwest China. *Miner. Depos.* **2004**, *23*, 464–472.
16. Wu, C.L.; Yang, J.S.; Yao, S.Z.; Zeng, L.S.; Chen, S.Y.; Li, H.B.; Qi, X.Q.; Wooden, J.L.; Mazdab, F.K. Characteristics of the granitoid complex and its zircon SHRIMP dating at the south margin of the Bashikaogong Basin, North Altun, NW China. *Acta Petrol. Sin.* **2005**, *21*, 846–858.
17. Yang, J.S.; Shi, R.D.; Wu, C.L.; Su, D.C.; Chen, S.Y.; Wang, X.B.; Wooden, J. Petrology and SHRIMP age of the Hongliugou ophiolite at Milan, north Altun, at the northern margin of the Tibetan plateau. *Acta Petrol. Sin.* **2008**, *24*, 1567–1584.
18. Zhang, F.; Wang, K.Q.; Yu, W.Q.; Yang, G.C. Geochemical characteristics and formation environment and epoch of volcanic rocks on the northern margin of Altun area, northwestern China. *Miner. Depos.* **2008**, *27*, 105–114.
19. Xu, Z.Q.; Yang, J.S.; Li, H.B.; Zhang, J.X.; Wu, C.L. *Orogenic Plateau: Terrane Amalgamation, Collision and Uplift in the Qinhai-Tibet Plateau*; Geological Publishing House: Beijing, China, 2007; pp. 1–458.
20. Han, F.B.; Chen, B.L.; Cui, L.L.; Wang, S.X.; Chen, Z.L.; Jiang, R.B.; Li, L.; Qi, W.X. Zircon SHRIMP U-Pb age of intermediate-acid intrusive rocks in Kaladawan area, eastern Altun Mountains, NW China, and its implications. *Acta Petrol. Sin.* **2012**, *28*, 2277–2291.
21. Liu, Y.; Hu, Z.; Gao, S.; Günther, D.; Xu, J.; Gao, C.; Chen, H. In situ analysis of major and trace elements of anhydrous minerals by LA-ICP-MS without applying an internal standard. *Chem. Geol.* **2008**, *257*, 34–43. [CrossRef]
22. Maréchal, C.N.; Télouk, P.; Albarède, F. Precise analysis of copper and zinc isotopic compositions by plasma-source mass spectrometry. *Chem. Geol.* **1999**, *156*, 251–273. [CrossRef]
23. Le Maitre, R.W.; Streckeisen, A.; Zanettin, B.; Le Bas, M.J.; Bonin, B.; Bateman, P. *Igneous Rocks: A Classification and Glossary of Terms: Recommendations of the International Union of Geological Sciences Subcommission on the Systematics of Igneous Rocks*, 2nd ed.; Cambridge University Press: Cambridge, UK, 2002.
24. Peccerillo, A.; Taylor, S.R. Geochemistry of eocene calc-alkaline volcanic rocks from the kastamonu area, northern turkey. *Contrib. Mineral. Petrol.* **1976**, *58*, 63–81. [CrossRef]
25. Dupuy, C.; Dostal, J. Trace element geochemistry of some continental tholeiites. *Earth Planet. Sci. Lett.* **1984**, *67*, 61–69. [CrossRef]

26. Sun, S.S.; Mcdonough, W.F. Chemical and isotopic systematics of oceanic basalts: Implications for mantle composition and processes. *Geol. Soc. Lond. Spec. Publ.* **1989**, *42*, 313–345. [CrossRef]
27. Mclennan, S.M. Relationships between the trace element composition of sedimentary rocks and upper continental crust. *Geochem. Geophys. Geosystems* **2001**, *2*. [CrossRef]
28. Rudnick, R.L.; Gao, S.; Holland, H.D.; Turekian, K.K. Composition of the continental crust. *Treatise Geochem.* **2003**, *3*, 1–64.
29. Baker, T.; Lang, J.R. Reconciling fluid inclusion types, fluid processes, and fluid sources in skarns: An example from the Bismark Deposit, Mexico. *Miner. Depos.* **2003**, *38*, 474–495. [CrossRef]
30. Wen, G.; Li, J.W.; Hofstra, A.H.; Koenig, A.E.; Lowers, H.A.; Adams, D. Hydrothermal reequilibration of igneous magnetite in altered granitic plutons and its implications for magnetite classification schemes: Insights from the Handan-Xingtai iron district, North China Craton. *Geochim. Cosmochim. Acta* **2017**, *213*, 255–270. [CrossRef]
31. Dare, S.A.S.; Barnes, S.J.; Beaudoin, G.; Méric, J.; Boutroy, E.; Potvin-Doucet, C. Trace elements in magnetite as petrogenetic indicators. *Miner. Depos.* **2014**, *49*, 785–796. [CrossRef]
32. Hu, H.; Li, J.W.; Lentz, D.; Ren, Z.; Zhao, X.F.; Deng, X.D.; Hall, D. Dissolution–reprecipitation process of magnetite from the Chengchao iron deposit: Insights into ore genesis and implication for *in-situ* chemical analysis of magnetite. *Ore Geol. Rev.* **2014**, *57*, 393–405. [CrossRef]
33. Hu, H.; Lentz, D.; Li, J.W.; Mccarron, T.; Zhao, X.F.; Hall, D. Reequilibration processes in magnetite from iron skarn deposits*. *Econ. Geol.* **2015**, *110*, 1–8. [CrossRef]
34. Makvandi, S.; Ghasemzadeh-Barvarz, M.; Beaudoin, G.; Grunsky, E.C.; Beth Mcclenaghan, M.; Duchesne, C. Principal component analysis of magnetite composition from volcanogenic massive sulfide deposits: Case studies from the Izok Lake (Nunavut, Canada) and Halfmile Lake (New Brunswick, Canada) deposits. *Ore Geol. Rev.* **2016**, *72*, 60–85. [CrossRef]
35. Dupuis, C.; Beaudoin, G. Discriminant diagrams for iron oxide trace element fingerprinting of mineral deposit types. *Miner. Depos.* **2011**, *46*, 319–335. [CrossRef]
36. Wang, C.M.; Zhang, L.; Tang, H.S.; Chen, H.Y.; Li, X.L.; Zheng, Y.; Li, D.F.; Fang, J.; Dong, L.H.; Qu, X. Genesis of the Kaladawan Fe–Mo ore field in Altyn, Xinjiang, China: Constraints from mineralogy and geochemistry. *Ore Geol. Rev.* **2017**, *81*, 587–601. [CrossRef]
37. Pons, J.; Franchini, M.; Meinert, L.; Recio, C.; Etcheverry, R. Iron skarns of the Vegas Peladas district, mendoza, argentina. *Econ. Geol.* **2009**, *104*, 157–184. [CrossRef]
38. Dauphas, N.; Zuilen, M.; Wadhwa, M.; Davis, A.; Marty, B.; Janney, P. Clues from Fe isotope variations on the origin of Early Archean BIFs from Greenland. *Science* **2004**, *306*, 2077–2080. [CrossRef] [PubMed]
39. Sun, J.; Zhu, X.K.; Chen, Y.L.; Fang, N. Iron isotopic constraints on the genesis of Bayan Obo ore deposit, Inner Mongolia, China. *Precambrian Res.* **2013**, *235*, 88–106. [CrossRef]
40. Dong, A.; Zhu, X.K.; Li, Z.H.; Kendall, B.; Li, S.Z.; Wang, Y.; Tang, C. A multi-isotope approach towards constraining the origin of large-scale Paleoproterozoic B-(Fe) mineralization in NE China. *Precambrian Res.* **2017**, *292*, 115–129. [CrossRef]
41. Sun, J.; Zhu, X.K.; Li, Z.H. Confirmation and global significance of a large-scale early Neoproterozoic banded iron formation on Hainan Island, China. *Precambrian Res.* **2018**, *307*, 82–92. [CrossRef]
42. Hanson, G.N. Rare earth elements in petrogenetic studies of igneous systems. *Annu. Rev. Earth Planet. Sci.* **1980**, *8*, 371–406. [CrossRef]
43. Ge, Z.H.; Han, F. Geochemistry of rare earth elements in the Makeng iron deposit. *Miner. Depos.* **1984**, *3*, 1–10.
44. Frietsch, R.; Perdahl, J.A. Rare earth elements in apatite and magnetite in Kiruna-type iron ores and some other iron ore types. *Ore Geol. Rev.* **1995**, *9*, 489–510. [CrossRef]
45. Zhang, Z.X.; Yang, F.Q.; Chai, F.M.; Liu, F.; Geng, X.X.; Lv, S.J.; Jiang, L.P.; Zhong, T.Z.; Ouyang, L.J. A study of REE geochemistry of Wutubulake iron deposit in Altay, Xin jiang. *Miner. Depos.* **2011**, *30*, 87–102.
46. Hu, H. Mineralogical, Geochemical, and Geochornologcal Constrains on the Genesis of Iron Deposits in the Daye District, Eastern China. Ph.D. Thesis, China University Of Geosciences, Wuhan, China, 2016.
47. Wang, Y.; Zhu, X.K.; Mao, J.W.; Li, Z.H.; Cheng, Y.B. Iron isotope fractionation during skarn-type metallogeny: A case study of Xinqiao Cu–S–Fe–Au deposit in the Middle–Lower Yangtze valley. *Ore Geol. Rev.* **2011**, *43*, 194–202. [CrossRef]
48. Bullen, T.D.; White, A.F.; Childs, C.W.; Vivit, D.V.; Schulz, M. Demonstration of significant abiotic iron isotope fractionation in nature. *Geology* **2000**, *29*, 699. [CrossRef]
49. Polyakov, V.B.; Mineev, S.D. The use of Mössbauer spectroscopy in stable isotope geochemistry. *Geochim. Cosmochim. Acta* **2000**, *64*, 849–865. [CrossRef]
50. Johnson, C.M.; Skulan, J.L.; Beard, B.L.; Sun, H.; Nealson, K.H.; Braterman, P.S. Isotopic fractionation between Fe(III) and Fe(II) in aqueous solutions. *Earth Planet. Sci. Lett.* **2002**, *195*, 141–153. [CrossRef]
51. Liang, J.X. *Experimental Study on the Formation Mechanism of Skarn and Skarn Deposits in China*; Xueyuan Publishing House Beijing: Beijing, China, 2000; pp. 152–192.
52. Meng, L.T.; Chen, B.L.; Zhao, N.N.; Wu, Y.; Zhang, W.G.; He, J.T.; Wang, B.; Han, M.M. The distribution, geochronology and geochemistry of early Paleozoic granitoid plutons in the North Altun orogenic belt, NW China: Implications for the petrogenesis and tectonic evolution. *Lithos* **2017**, *268*, 399–417. [CrossRef]
53. Zhu, B.; Zhang, H.F.; Zhao, X.M.; He, Y.S. Iron isotope fractionation during skarn-type alteration: Implications for metal source in the Han-Xing iron skarn deposit. *Ore Geol. Rev.* **2016**, *74*, 139–150. [CrossRef]

54. Chou, I.M.; Eugster, H.P. Solubility of magnetite in supercritical chloride solutions. *Am. J. Sci.* **1977**, *277*, 1296–1314. [CrossRef]
55. Chen, Y.; Zhang, Z.C. Study on source, transport and the enrichment mechanism of iron in iron skarn deposits. *Rock Miner. Anal.* **2012**, *31*, 889–897.